Molecular dynamics of the wetting and drying of a wall with a long-ranged wall-fluid interaction

Molecular dynamics of the wetting and drying of a wall with a long-ranged wall–fluid interaction

M J P Nijmeijer†, C Bruin†, A F Bakker† and J M J van Leeuwen‡

† Laboratorium voor Technische Natuurkunde, PO Box 5046, 2600 GA Delft,
The Netherlands
‡ Instituut Lorentz, PO Box 9506, 2300 RA Leiden, The Netherlands

Abstract. We have studied the influence of a long-ranged force between a wall and a fluid on the wetting properties of the wall–fluid system. The system with short-ranged forces, i.e. cut-off Lennard-Jones potentials only, has been studied extensively in previous simulations, revealing the presence of a wetting and a drying transition. We have increased the cut-off radius of the wall–fluid potential by a factor of 5 in the simulations and re-inspected these transitions. The wetting transition turns out not to be much affected by the long-ranged potential but the drying transition is suppressed.

1. Introduction

The intermolecular forces in simple fluids are long-ranged and their tails are usually described by attractive potentials which decay as $\sim 1/r^6$ where r denotes the intermolecular distance. Although weak beyond a certain distance, e.g. 2.5 molecular diameters, this tail can have a significant influence on the properties of a fluid, especially near an interface. This has been demonstrated in simulations of coexisting liquid and vapour phases [1] and of the interface between them [2] as well as by density-functional studies [3] of such interfaces. They show that an increase of the interaction range between the fluid particles drastically alters the properties of the co-existing phases and of the interface between them. It can be expected that similar changes will occur at the interface between a fluid and a wall upon the increase of the interparticle interaction range [4]. The influence of the tails of the potentials on a wall–fluid interface is of special interest in the vicinity of a surface phase transition such as the wetting or drying transition—for a review see e.g. [5]. Such transitions may be sensitive to small perturbations of the interaction potentials and although a quantitative estimate of the effect of the attractive tails is hard to give, mean field theories [6–8] indeed predict them to have a dominant influence on the transitions. It is difficult to control the interparticle forces in an experiment but it has been attempted by chemically modifying the experimental system [9]. On the contrary, the interparticle potentials are completely controlled in simulations but they can usually treat short-ranged forces only, as we will discuss below.

The long-ranged fluid–fluid interactions play a subtle role in the properties of a wetting or a drying transition but the influence of the long-ranged wall–fluid interaction in a system with short-ranged fluid–fluid forces can be understood more easily.

The attractive long-ranged tail will facilitate the occurrence of a wetting transition in such a system while the drying transition is expected to disappear completely. In other words, in the absence of the tail, a liquid slab which is adsorbed at the wall can wander away freely when it detaches. Thus a vapour layer near the wall can be of arbitrary thickness. In the presence of the tail, the slab will be attracted to the wall at all distances. The slab may be repelled from the wall by the short-ranged wall–fluid interactions but since it will no longer experience these if it is far enough from the wall, the attractive tail will always tend to keep the slab at a finite distance. So only a microscopically thin layer of vapour near the wall is possible and thus, the system cannot be completely dry.

Simulations have difficulties in treating the long-ranged attractive tails. An increase of the interaction range strongly increases the number of interactions that has to be evaluated in the calculation. The simulations are slowed down considerably, the number of interactions being proportional to $\sim r_c^3$ in three dimensions, where r_c is the interaction range. Furthermore, the boundary conditions, e.g. periodic boundaries, may lead to pathological interactions if the range gets larger than the system size. Therefore, the potentials used in simulations are usually either short-ranged by definition, e.g. hard-sphere potentials, or truncated. In the case of the Lennard-Jones potential, given by

$$\phi(r) = 4\epsilon[(\sigma/r)^{12} - (\sigma/r)^6] \tag{1}$$

a cut-off length $r_c = 2.5\sigma$ is often used (σ is the length scale, ϵ the energy scale of the interaction) although e.g. a cut-off of at least 5σ was used in a recent study of pre-wetting [10]. Such truncated potentials are usually shifted in molecular-dynamics simulations to remove the discontinuity in the potential at the truncation point.

Extensive simulation studies of the wetting and drying of a substrate by a fluid were carried out by Henderson and van Swol [11] and by Sikkenk *et al* and the present authors [12–15]. The latter series of simulations studied the wetting and drying of a wall built of a lattice of solid particles. As in the simulations of Henderson and van Swol, short-ranged interactions were used throughout. The wetting and drying transition were induced by changing the solid–fluid interaction strength ϵ_{sf}: it turned out that the solid–liquid interface becomes unstable at low values of ϵ_{sf} whereas the solid–vapour interface becomes unstable at high values. In the former case, a vapour layer intrudes between the solid and the liquid phase, i.e. a drying transition occurs. Similarly, in the latter case, a liquid layer intrudes between the solid and the vapour phase as is characteristic of a wetting transition. The wetting and drying of the wall were studied by an inspection of density profiles, surface free energies and contact angles θ. To be specific, θ is the angle with which the meniscus of a droplet placed on a solid substrate meets the substrate [16, 17]. It is a convenient parameter to characterize the wetting state of the wall as it decreases continuously from $\theta = \pi$ for a completely dry wall to $\theta = 0$ for a completely wet wall with increasing ϵ_{sf}. Moreover, the way in which θ approaches its limiting values $\theta = 0$ and $\theta = \pi$ reflects the order of the corresponding transition—for a review see e.g. [5]. The most accurate results on the location and order of the wetting and drying transition were obtained in the last of the previous simulations [15] in which the solid particles that form the wall were frozen in at their lattice positions, thus forming an external potential for the fluid. The derivative $\partial\cos\theta/\partial\epsilon_{sf}$ was measured and it revealed a surprising difference in character between the wetting and the drying transition: whereas the

wetting transition appeared to be strongly first-order, the drying transition exhibited a continuous character. This observation, however, is debated by Henderson and van Swol [11] who find the drying transition to be of a 'fluctuation-induced' first-order character.

The wetting properties may vary considerably when the cut-off length r_c grows larger, thereby giving the simulations a more realistic character. When all interaction ranges increase, the computing time increases prohibitively and therefore we allow only a larger wall–fluid interaction range. If the solid particles are fixed at their lattice positions and the lattice structure of the wall is neglected at distances z larger than r_c from the wall, the influence of the wall beyond r_c is described by a structureless external potential. Such a relatively simple external potential can be added to the simulations without a dramatic increase of computing time and is a step closer to the situation encountered in reality.

Since the last of the previous simulations [15] used an inert wall and moreover, gave the most accurate results for the location and order of the wetting and drying transition, we use the same measurement procedure while adding the long-ranged potential. We simulate a fluid at liquid–vapour coexistence enclosed between two parallel substrate walls with one wall covered with liquid, the other with vapour. The liquid and vapour phase meet in a liquid–vapour interface between the two walls. This configuration allows one to measure the density profiles, the surface tensions and the derivatives of the latter with respect to ϵ_{sf} simultaneously for the solid–liquid, solid–vapour and the liquid–vapour interface. The systems are studied at various values of the wall–fluid affinity ϵ_{sf} while the temperature is kept fixed. A change in ϵ_{sf} alters the properties of the solid–fluid interfaces but it should not affect the properties of the bulk liquid and vapour phase and of the interface between them. The cosines of the contact angle θ and the derivatives $\partial \cos \theta / \partial \epsilon_{sf}$ are calculated from the measurements of the surface tensions γ and their derivatives $\partial \gamma / \partial \epsilon_{sf}$ [11] and the application of Young's law [18]

$$\cos \theta = \frac{\gamma_{sv} - \gamma_{sl}}{\gamma_{lv}} \tag{2}$$

with γ_{sl}, γ_{sv} and γ_{lv} the surface tensions of the solid–liquid, solid–vapour and liquid–vapour interface respectively. From the behaviour of the density profiles, $\cos \theta$ and $\partial \cos \theta / \partial \epsilon_{sf}$ the occurrence of a wetting and a drying transition are inspected. As we discussed above, it is expected that the addition of the tail of the solid–fluid potential suppresses the drying transition while the wetting transition should occur at a lower value of ϵ_{sf}.

This paper is further arranged as follows. The organization and the technical aspects of the simulation are described in the next section. The obtained density profiles are discussed in section 3. The measurements of the surface tensions, their derivatives with respect to ϵ_{sf} and the results for $\cos \theta$ and $\partial \cos \theta / \partial \epsilon_{sf}$ are discussed in section 4. The paper closes with a discussion in section 5.

2. Description of the system

The simulations are set up in the same way as before [14,15] apart from the fact that a long-ranged wall–fluid potential has been added. We summarize the main

features and refer to Nijmeijer *et al* [14] for a more elaborate description. The fluid is enclosed in a three-dimensional box with periodic boundary conditions in all directions. The wall is built from three layers of an FCC lattice, placed in the x–y plane. The interaction between the particles of type A and B is of the Lennard-Jones 12-6 type, characterized by σ_{AB} and ϵ_{AB} and truncated at $2.5\sigma_{AB}$ where A and B stand for either 'solid' or 'fluid'. At this point we have to mention that also in previous work [12–15] a cut-off length of $2.5\sigma_{sf}$ for the solid–fluid interaction has been reported but that, unfortunately, this cut-off length has been $2.35\sigma_{sf}$ instead. In this work, however, we have restored the cut-off length of the solid–fluid interaction at $2.5\sigma_{sf}$. The potentials are shifted such that they are continuous at the truncation point. The system contains 2904 solid particles throughout and 8400 fluid particles in most of the simulations but some simulations have been carried out with 7297 fluid particles. The box has a length $L = 29.1\sigma_{ff}$. The temperature is kept fixed at $T^* = k_BT/\epsilon_{ff} = 0.9$ and the main parameter in the simulations is ϵ_r, defined by $\epsilon_r = \epsilon_{sf}/\epsilon_{ff}$. For the reduced timestep we again used the value of 0.01. The DMDP simulations were carried out on the Delft molecular dynamics processor (DMDP) [19] which is especially designed for molecular-dynamics calculations.

The external potential ϕ^{ext} which represents the solid–fluid interaction [20] consists of two parts:

$$\phi^{ext}(r) = \phi^{ext}_{sr}(r) + \phi^{ext}_{lr}(z) \tag{3}$$

with the short-ranged part defined as previously [14, 15]

$$\phi^{ext}_{sr}(r) = \sum_l \phi_{sf}(|r - a_l|) \tag{4}$$

where ϕ_{sf} denotes the truncated and shifted Lennard-Jones interaction between a solid and a fluid particle and the sum is over all solid particles, a_l being the lattice position of solid particle l. We chose σ_{sf} as $\sigma_{sf} = 0.941\sigma_{ff}$ which is between σ_{ff} and σ_{ss} ($\sigma_{ss} = 0.847\sigma_{ff}$) to prevent solidification of the first adsorbed fluid layers. The lattice structure is neglected in the additional long-ranged potential ϕ^{ext}_{lr} which acts at distances larger than $2.5\sigma_{sf}$ away from the wall only. It is constructed by smearing out the wall particles homogeneously over the wall with density n_s which equals for our FCC lattice $n_s = 1.05/\sigma^3_{ss}$ (this implies a reduced density $n^*_s = n_s\sigma^3_{ff} = 1.73$). The long-ranged potential thus becomes the Lennard-Jones 9-3 potential between a fluid particle and a half infinite solid continuum. The fluid is enclosed in the z-direction between the outer layers of the wall and is thus attracted to one outer layer within a certain distance from it and to the other one in the remaining part of the box. If we place the origin $z = 0$ in the middle of the fluid between the outer layers of the wall such that z ranges from $-L/2$ to $L/2$ (as in figures 1–3) we have for the long-ranged part of the potential

$$\phi^{ext}_{lr}(z) = \begin{cases} \phi^L_{lr}(z) & -L/2 < z < z_m \\ \phi^R_{lr}(z) & z_m < z < L/2 \end{cases} \tag{5}$$

with the turning point z_m chosen at $z_m = 0$ unless stated otherwise. The potential ϕ^L_{lr} acts on the left of the system and attracts the fluid particles to the left outer layer

of the wall

$$\phi_{lr}^L(z) = \begin{cases} \frac{2}{3}\pi n_s \sigma_{sf}^3 \epsilon_{sf} \left[\frac{2}{15} \left(\frac{1}{2.5} \right)^9 - \left(\frac{1}{2.5} \right)^3 \right] & -\frac{L}{2} < z < -z_l + 2.5\sigma_{sf} \\ \frac{2}{3}\pi n_s \sigma_{sf}^3 \epsilon_{sf} \left[\frac{2}{15} \left(\frac{\sigma_{sf}}{z + z_l} \right)^9 - \left(\frac{\sigma_{sf}}{z + z_l} \right)^3 \right] & -z_l + 2.5\sigma_{sf} < z < z_m \end{cases}$$

(6)

where the outer layers are located at $z = -z_l$ and $z = z_l$ (with $z_l = 13.89\sigma_{ff}$ in our simulations). The potential ϕ_{lr}^R acts at the right of the system and attracts the fluid to the right outer layer but is furthermore defined analogously to ϕ_{lr}^L. The wall–fluid potential ϕ^{ext} therefore has a range of $13.89\sigma_{ff}$ away from the outer layer of the wall for the usual choice $z_m = 0$. Note that as ϕ_{sr}^{ext} and ϕ_{lr}^{ext} are continuous throughout the computational box, their sum ϕ^{ext} is continuous as well. The update of the particle velocities that incorporates the long-ranged potential cannot be done on the DMDP since this computer was not designed to handle such forces. The DMDP, however, is connected to an array processor where this velocity update is performed and the pressure tensor (see below) is measured. By this construction, the long-ranged potential ϕ_{lr}^{ext} could not be applied each timestep. Instead, the fluid was subject to the long-ranged force each 15th timestep with the force 15 times as large as it would be had it been applied each timestep.
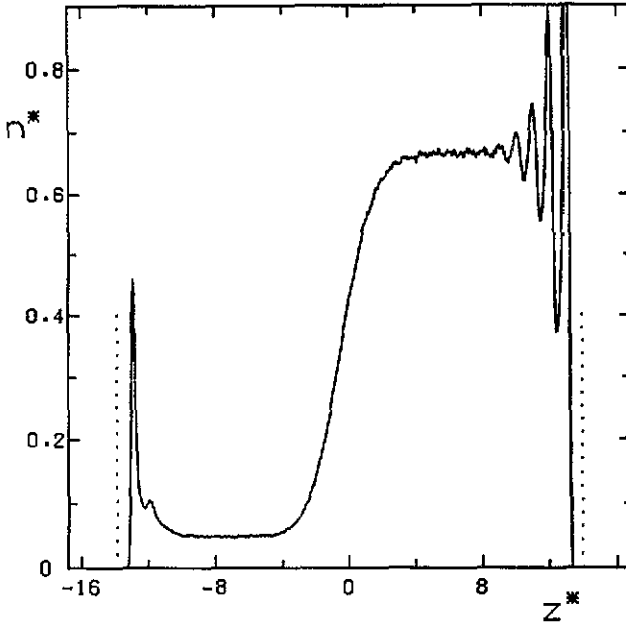

Figure 1. Density profile at $\epsilon_r = 0.5$, $N_f = 8400$ obtained as an average over 2000 particle configurations. The dotted lines denote the positions of the outer layers of the wall.

The solid–fluid surface tensions γ_{sf} and their derivatives $\partial\gamma_{sf}/\partial\epsilon_{sf}$ are measured in the same way as before [14, 15]:

$$\gamma_{sf} = \frac{1}{L^2} \int_{-L/2}^{L/2} dx\, dy \int_0^{z_b} dz \left(p_N(z) - p_T(z) - n(r) z \frac{\partial}{\partial z} \phi^{ext}(r) \right)$$
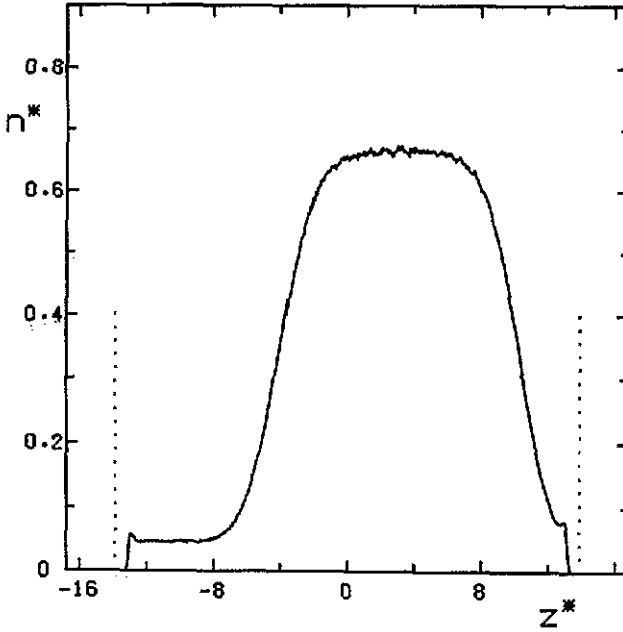
(7)

Figure 2. Density profile at $\epsilon_t = 0.1$, $N_f = 8400$ obtained as an average over 2000 particle configurations. The dotted lines denote the positions of the outer layers of the wall.
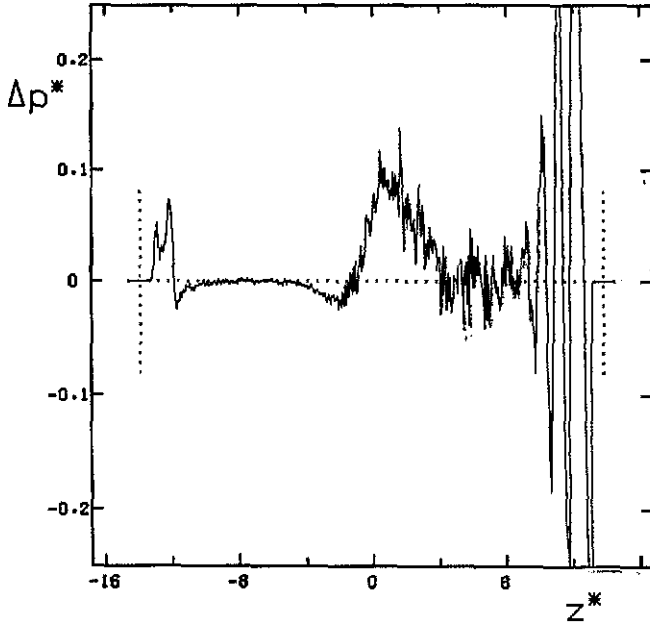

Figure 3. Pressure difference profile $\Delta p = p_N - p_T$ in reduced units $\Delta p^* = \Delta p \sigma_{ff}^3 / \epsilon_{ff}$ at $\epsilon_t = 0.5$, $N_f = 8400$, obtained as an average over 1000 configurations.

$$\frac{\partial \gamma_{sf}}{\partial \epsilon_{sf}} = \frac{1}{L^2} \int_{-L/2}^{L/2} dx\, dy \int_0^{z_b} dz\, n(\mathbf{r}) \frac{\phi^{ext}(\mathbf{r})}{\epsilon_{sf}} \tag{8}$$

where the origin $z = 0$ is placed at the middle wall layer for the moment and the

fluid is imagined to be at $z > 0$; p_N denotes the component of the pressure tensor normal to the surface, p_T the tangential component and n stands for the local density of the fluid. In principle, the integrations over z should range from 0 to ∞ but in the finite geometry of the box the integral has to be truncated at a position z_b which is a position in the bulk of the fluid. The precise location of z_b does not matter in the absence of ϕ_{lr}^{ext} since the integrands of (7) and (8) vanish in the bulk fluid in that case. Including ϕ_{lr}^{ext}, however, the integrand vanishes only at $z_b = \infty$ even if the fluid is of a bulk character already at a finite distance from the wall because ϕ_{lr}^{ext} itself vanishes only infinitely far away from the wall. The solid–fluid surface tension one measures as well as its derivative with respect to ϵ_{sf} depend therefore on the choice of z_b. The effect of the truncation at z_b can be estimated if one assumes that the fluid is of a bulk character at distances larger than z_b away from the wall, an assumption which is reasonable for our simulations. In that case the difference $(p_N - p_T)$ vanishes and the local density is equal to the bulk density n_b at z larger than z_b. Extending integral (7) over z to infinity, one then adds a correction $\Delta\gamma_{sf}$ to γ_{sf} given by

$$\Delta\gamma_{sf} = -n_b \frac{1}{L^2} \int_{-L/2}^{L/2} dx\,dy \int_{z_b}^{\infty} dz\, z \frac{\partial}{\partial z} \phi^{ext}(r) \tag{9}$$

Similarly we estimate the correction $\Delta\partial\gamma_{sf}/\partial\epsilon_{sf}$ to $\partial\gamma_{sf}/\partial\epsilon_{sf}$ to be

$$\Delta\frac{\partial\gamma_{sf}}{\partial\epsilon_{sf}} = n_b \frac{1}{L^2} \int_{-L/2}^{L/2} dx\,dy \int_{z_b}^{\infty} dz\, \frac{\phi^{ext}(r)}{\epsilon_{sf}} . \tag{10}$$

In the case of the Lennard-Jones 9-3 potential, the corrections take the explicit form (since z_b is always chosen further than $2.5\sigma_{sf}$ away from the outer wall layer so that ϕ^{ext} is given by ϕ_{lr}^{ext} in (9) and (10)):

$$\Delta\gamma_{sf} = -2\pi n_b n_s \sigma_{sf}^6 \epsilon_{sf} \left(\frac{1}{2(z_b - z_l)^2} + \frac{z_l}{3(z_b - z_l)^3} \right) \tag{11}$$

$$\Delta\frac{\partial\gamma_{sf}}{\partial\epsilon_{sf}} = -\frac{\pi}{3} n_b n_s \sigma_{sf}^4 \left(\frac{\sigma_{sf}}{z_b - z_l} \right)^2 \tag{12}$$

Note that since the origin $z = 0$ is placed at the middle wall layer in equations (9) and (10), the position of the outer wall layer z_l in (11) and (12) equals $z_l = 0.66\sigma_{ff}$. Furthermore, the repulsive term of ϕ^{ext} has been neglected in (11) and (12).

3. The density profiles

As starting configurations we either used a configuration of our previous simulations [15] with the same ϵ_r and applied the long-ranged potential to it or we took a configuration at different ϵ_r for which the external potential had been applied and then changed ϵ_r. Most systems were equilibrated in some 15 600 timesteps whereupon no systematic evolution of the potential energy, the density profile or the pressure tensor profile was observed. After this equilibration, we sampled during 30 000 timesteps 2000 configurations of each system to determine the particle density and pressure

tensor profile. Thus, the configurations were sampled each 15th timestep. Error bars in the data denote the standard deviation as calculated from sub-averages over 200 configurations each. We paid special attention to the centre of mass motion, the so called 'drift', which is partly caused by the finite numerical accuracy of the molecular-dynamics calculation. It is customary in molecular-dynamics simulations to set the total momentum of the fluid regularly to zero in order to prevent the drift from becoming too large. Since, however, the dynamics of the liquid slab perpendicular to the wall is a probe of the wetting and drying characteristics, we did not want to affect the momentum of the fluid in the z-direction but only to set the fluid's momentum in the x- and y-direction regularly (i.e. every 3000 timesteps) to zero [11]. Figure 1 shows a particle density profile at $\epsilon_r = 0.5$.

In this way, we scanned a range of ϵ_r values between $\epsilon_r = 0.2$ and $\epsilon_r = 0.7$ where the latter value turned out to be well above the wetting transition. The region $\epsilon_r < 0.2$, in which the contact angles approached the drying limit $\theta = \pi$, was inspected in greater detail. This regime was accessed by starting with an equilibrated particle configuration at $\epsilon_r = 0.2$ and decreasing ϵ_r via $\epsilon_r = 0.15$ and $\epsilon_r = 0.10$ to the lowest value we inspected: $\epsilon_r = 0.05$. The liquid layer shifts away from the wall while decreasing ϵ_r and it becomes increasingly hard to tell whether the solid–liquid interface should be regarded as an interface bound to the wall or as consisting of a solid–vapour and a free liquid–vapour interface (see figure 2). Moreover, the position of this weakly bound liquid slab starts to fluctuate at such values of ϵ_r which causes large fluctuations in especially the $\partial \gamma_{sl}/\partial \epsilon_{sf}$ data: when the slab moves closer to the wall the number of particles in the first adsorbed layer increases and $\partial \gamma_{sl}/\partial \epsilon_{sf}$ drops while the opposite occurs when the slab moves a little away from the wall. It has been suggested [11] that these fluctuations are significantly suppressed by the presence of the opposite wall since the vapour phase between the liquid slab and the opposite wall becomes small at these very low values of ϵ_r. We checked this by reducing at $\epsilon_r = 0.05$ the number of fluid particles to 7297, thereby thinning the liquid slab and increasing the length of the vapour phase. From this point on, we increased ϵ_r to $\epsilon_r = 0.10$ and subsequently to $\epsilon_r = 0.15$, followed by a decrease of ϵ_r via $\epsilon_r = 0.10$ back to $\epsilon_r = 0.05$. In all these cases, the simulation at the next value of ϵ_r was started from the last configuration obtained at the previous ϵ_r. In this way we obtained a branch of increasing and a branch of decreasing ϵ_r for the system with the reduced amount of fluid particles.

A first question is whether the bulk phases are affected by the wall–fluid interaction or not. Compared with the previous case [14, 15], this question is more stringent now since the fluid experiences the external field everywhere in the system. A first criterion for the bulk character of a phase is the presence of a homogeneous density. The local density fluctuates around a mean value in the region where we locate the liquid and vapour phase respectively (see figure 1). The size of these regions is approximately the same as previously [14, 15] and the mean density around which the local density fluctuates does not vary systematically with ϵ_r. Averaged over all ϵ_r, taking only the systems with $N_f = 8400$ fluid particles into account, the reduced liquid and vapour density are $n_l^* = 0.6642 \pm 0.0004$ and $n_v^* = 0.0461 \pm 0.0005$ (with $n^* = n\sigma_{ff}^3$) which coincides with former results [14, 15, 1]. A second criterion for the presence of a bulk phase is the vanishing of $[p_N(r) - p_T(r)]$. Figure 3 shows this difference Δp in the asymmetric system at $\epsilon_r = 0.5$ from which it is seen that Δp vanishes in the liquid and in the vapour phase. The liquid–vapour surface tension γ_{lv}, defined as the integral over $\Delta p(z)$ from well within the bulk vapour phase into

the bulk liquid phase, is listed in table 1 as it is obtained at the various values of ϵ_r. It does not vary systematically with ϵ_r and its average over ϵ_r equals $\gamma_{lv}^* = 0.221 \pm 0.005$ which agrees well with previous results. Finally, we consider the pressure which is measured in the same way as before [14]. Its value in the various systems is listed in table 1 which again shows no systematic variation of p^* with ϵ_r. When averaged over all ϵ_r, it equals $p^* = 0.0309 \pm 0.0003$ which again agrees with our previous results [14]. Therefore we conclude that also in the presence of the long-ranged field it is possible to identify a liquid and a vapour phase with properties that cannot be distinguished from the field-free case.

Table 1. Liquid–vapour surface tension and pressure as measured in the systems with different wall–fluid affinities ϵ_r. All quantities are in reduced units. The figures between parentheses denote the uncertainty (1 standard deviation) in the last one or two digits. The results are for the systems with 8400 fluid particles.

ϵ_r	γ_{lv}^*	p^*
0.05	0.236(10)	0.0319(4)
0.10	0.227(13)	0.0309(6)
0.15	0.236(9)	0.0316(3)
0.20	0.196(17)	0.0311(4)
0.25	0.223(12)	0.0307(6)
0.30	0.212(14)	0.0306(5)
0.40	0.194(8)	0.0312(4)
0.50	0.224(13)	0.0321(7)
0.60	0.233(10)	0.0298(7)
0.70	0.225(6)	0.0295(3)

The solid–fluid interfaces experience the presence of the long-ranged potential much stronger. The amount of particles adsorbed at the wall is clearly increased by this potential as can be seen from the figures 4 and 5 which show the reduced coverage $\Gamma^* = \Gamma \sigma_{ff}^2$ of the solid–vapour and solid–liquid interface for the systems without [14, 15] and the systems with the long-ranged wall–fluid potential. The coverage Γ of a solid–fluid interface is defined as

$$\Gamma = \frac{1}{L^2} \int_{-L/2}^{L/2} dx\, dy \int_0^{z_b} dz [n(r) - n_b] \tag{13}$$

with $n(r)$ the local density at position r and n_b the bulk density of the fluid. The coverage depends on the location of the origin $z = 0$ which we have chosen rather arbitrarily at the middle layer of the wall.

In case of the solid–vapour interface (figure 4), the difference in coverage between the two types of systems grows with increasing ϵ_r, reflecting the growing strength of the attractive long-ranged potential. The difference however, becomes significant beyond $\epsilon_r \approx 0.4$ only which is already close to the wetting transition [14, 15]. The solid–vapour interface is metastable above the transition and a liquid layer should intrude between the vapour and the wall. The simulations give some indication of this intrusion since we observe a slow drift in the solid–vapour coverage towards larger coverages at $\epsilon_r = 0.6$ and 0.7 in the systems with a long-ranged potential. The same effect is observed at $\epsilon_r = 0.8$ in the system with short-ranged interactions only.

The situation is reversed at the solid–liquid interface (figure 5): the difference in coverage grows for decreasing ϵ_r. This must be due to the approach of the drying
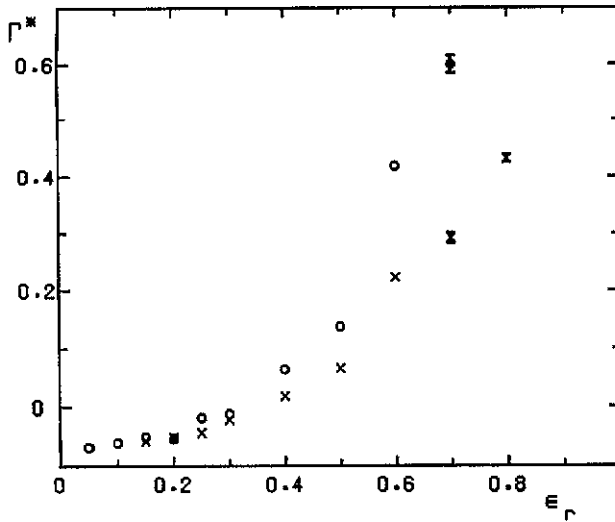
Figure 4. Coverage Γ of the solid–vapour interface in reduced units $\Gamma^* = \Gamma \sigma_{ff}^2$ as a function of ϵ_r. The crosses are the coverages for an interface with the interaction between a solid and a fluid particle truncated at $2.35\sigma_{sf}$ [14], the open circles are obtained in this work with $N_f = 8400$. When error bars are omitted they are of the order of the symbol size.
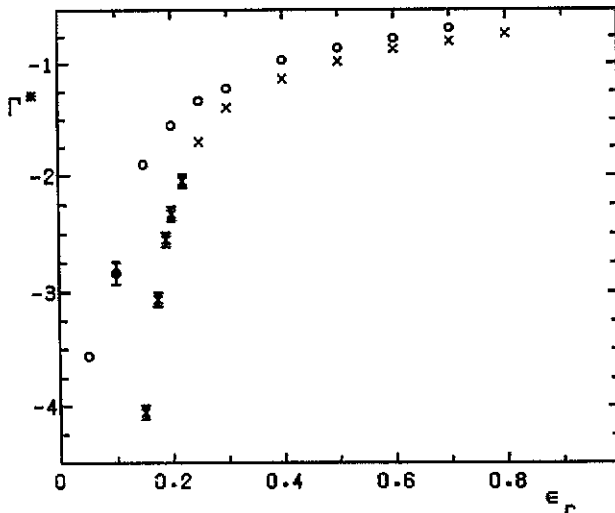

Figure 5. Coverage Γ of the solid–liquid interface. The symbols are as in figure 4.

transition. Near the transition, the liquid layer is weakly bound to the wall and sensitive to small changes in the external field. The liquid layer is tightly bound to the wall at large ϵ_r and the addition of a weak long-ranged interaction then turns out to have little influence on the structure of the interface.

The branches of increasing and decreasing ϵ_r with $N_f = 7297$ show no signs of hysteresis and the results compare reasonably well with the results for the system with $N_f = 8400$. Increasing ϵ_r from 0.05 to 0.1, the liquid slab initially remained too far (i.e. compared with the density profile for $N_f = 8400$) from the adsorbing side

of the substrate. After approximately 40 000 timesteps however, it moved closer to the adsorbing substrate while its actual position fluctuated strongly in the meantime. The liquid slab remained, while fluctuating, near the substrate for the next 50 000 timesteps we followed it. The coverage of the solid–liquid interface thus became $\Gamma^* = -2.8 \pm 0.1$ which is precisely the same value as obtained in the system with $N_f = 8400$. Increasing ϵ_r to 0.15 we again obtain good correspondence with the results for $N_f = 8400$ ($\Gamma^* = -2.00 \pm 0.04$ for $N_f = 7297$ and $\Gamma^* = -1.90 \pm 0.04$ for $N_f = 8400$). Lowering ϵ_r back to 0.1 we find that the liquid slab remains somewhat closer to the substrate as it did at $\epsilon_r = 0.1$ of the increasing branch ($\Gamma^* = -2.41 \pm 0.06$ averaged over 39 000 timesteps) but in view of the strong fluctuations in the slabs position we do not consider this as significant. The results at $\epsilon_r = 0.05$ for the branch of increasing ϵ_r, the branch of decreasing ϵ_r and the system with $N_f = 8400$ are again in good agreement ($\Gamma^* = -3.4 \pm 0.1$, -3.6 ± 0.1 and -3.56 ± 0.02 respectively). We thus conclude that even at these very low values of ϵ_r we obtain reproducable density profiles although the fluctuations at the solid–liquid interface become large. Moreover, we find no indications that a too small spacing between the sides of the substrate would prevent the liquid slab from desorbing from the substrate.

To obtain a better idea of the strength with which the liquid-slab is bound to the substrate by the long-ranged potential, we carried out a simulation (at $\epsilon_r = 0.10$ with $N_f = 7297$) in which we shifted the midpoint z_m. Starting with a configuration of the increasing branch at $\epsilon_r = 0.10$ (in which the liquid slab is adsorbed at the right-hand side of the substrate—see figure 6), we shifted z_m from $z_m^* = 0$ to $z_m^* = 10$. This increases the interaction range of the left-hand side of the substrate to $23.89\sigma_{ff}$ and the liquid slab, which is close to the right-hand side, becomes attracted to the left-hand side. As a result, we observe that the liquid slab moves a little away from the wall it is adsorbed at (the coverage of the solid–liquid interface drops to $\Gamma^* = -3.92 \pm 0.08$ which is an average over 45 000 timesteps), see figure 6. This is due to the fact that it no longer experiences the attractive long-ranged force of the side of the substrate it is adsorbed at. One would even expect that eventually the liquid slab should cross the system and becomes adsorbed at the opposite side since it is now attracted by this side. The attraction, however, is very weak when the liquid slab is as far away from the left-hand side of the substrate as in figure 6. For a particle placed at $z^* = 5.8$, the long-ranged tail of the left-hand side causes at $\epsilon_r = 0.1$ a velocity change that can just be represented in the 32 bits which the DMDP uses for the velocities. As the positions are given in 24 bits, however, the acquired velocity change will not immediately lead to a change in position. Only after approximately 4500 timesteps, the velocity has grown by such an amount that the least significant position bit will change. It is therefore dubious whether one should expect the crossing to occur within the 45 000 timesteps we followed the system.

Besides a shift in z_m^* to $z_m^* = 10$, we inspected the effect of a shift in z_m^* to $z_m^* = -10$. The starting configuration is the same as the one used in the simulation with the shift to $z_m^* = 10$. In the case that z_m^* is placed at -10, one expects that the liquid slab moves closer to the right-hand side, because it is attracted to this side over a larger distance. This is however not clearly observed: the slab shows some tendency to approach this side a little closer but in view of the large fluctuations in the slab's position it is not clear whether this tendency is a systematic effect. As the wall–fluid interaction is very weak at distances larger than $13.89\ \sigma_{ff}$, it is not surprising that the shift in z_m^* to $z_m^* = -10$ has little effect on the liquid phase in the system.
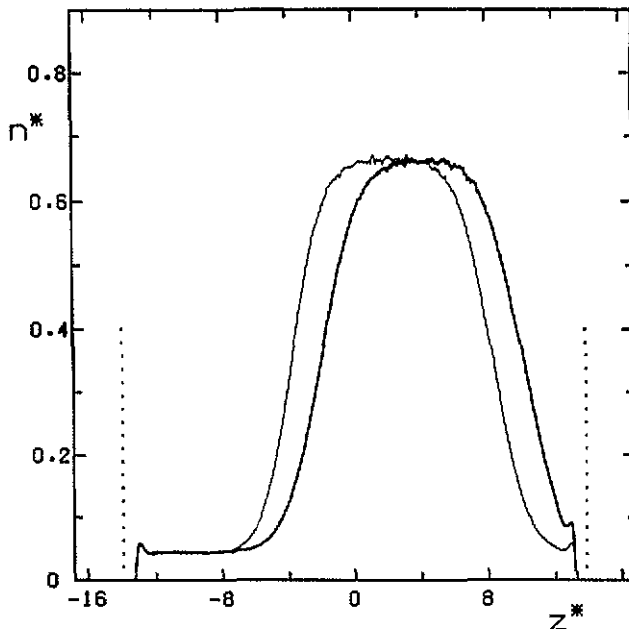
Figure 6. Two density profiles at $\epsilon_r = 0.10$, $N_f = 7297$. The thick curve shows the profile of the branch of increasing ϵ_r with $z_m^* = 0$. Shifting z_m^* to 10, the profile evolves to the profile shown by the thin curve. The thick profile is an average over 4000 partice configurations, the thin profile over 2600 configurations.

4. The contact angles

As mentioned above, an accurate way to determine the location of the drying transition has proved to be a direct measurement of the derivative of $\cos\theta$ with respect to ϵ_{sf}. These measurements are listed in table 2 and plotted in figure 7. The figure shows that the derivative smoothly vanishes on the approach $\epsilon_r = 0$ while it remains finite on the approach of the wetting transition which is located at $\epsilon_r \approx 0.5$ as we will see. The derivative decreases slowly above the wetting transition which is reminiscent of the sudden jump to $\partial\cos\theta/\partial\epsilon_{sf} = 0$ which should occur in a fully equilibrated system in the case of a first-order wetting transition. This jump, however, resulting from the spontaneous formation of a liquid layer at the solid–vapour interface, does not occur in the simulations [11, 14, 15]. Instead, the system is trapped in a metastable state when ϵ_r is increased above the wetting point: the liquid layer that should appear at the solid–vapour interface does not fully develop.

The slight differences in the coverage of the solid–liquid interface between the branch of increasing and the branch of decreasing ϵ_r at $\epsilon_r = 0.1$ and between the two system sizes at $\epsilon_r = 0.15$, also appear in the $\partial\cos\theta/\partial\epsilon_{sf}$ data. We attribute them to the large fluctuations in the sub-averages of the $\partial\cos\theta/\partial\epsilon_{sf}$ data which make it difficult to obtain accurate averages [15].

Altogether, figure 7 closely resembles the figure [15] for the case without the long-ranged potential except that in the present case it is hard to determine whether the drying point $\partial\cos\theta/\partial\epsilon_{sf} = 0$ is reached at a finite ϵ_r or not. We estimated a drying transition at $\epsilon_d = 0.169 \pm 0.005$ for the system without the long-ranged wall–fluid potential (and $r_c = 2.35\sigma_{sf}$ for the solid–fluid interaction) which is definitely at a larger ϵ_r than where one would estimate a possible drying transition in the present

Table 2. Solid–fluid surface tensions, cosines of the contact angles and their derivatives with respect to ϵ_r as measured at different ϵ_r. All quantities are in reduced units. The figures between parentheses denote the uncertainty (1 standard deviation) in the last one or two digits. The data for the branch of increasing and decreasing ϵ_r are displayed separately, the system at $\epsilon_r = 0.15$ has been added to the increasing branch.

ϵ_r	γ_{sl}^*	γ_{sv}^*	$\partial\gamma_{sl}^*/\partial\epsilon_r$	$\partial\gamma_{sv}^*/\partial\epsilon_r$	$\cos\theta$	$\partial\cos\theta/\partial\epsilon_r$
$N_f = 7297$, increasing ϵ_r						
0.05	0.261(8)	0.0408(6)	−0.126(4)	−0.069(2)	−0.98(3)	0.25(2)
0.10	0.252(5)	0.0386(7)	−0.249(19)	−0.103(2)	−0.95(2)	0.65(9)
0.15	0.245(11)	0.0331(10)	−0.501(17)	−0.128(2)	−0.94(5)	1.65(7)
$N_f = 7297$, decreasing ϵ_r						
0.05	0.273(12)	0.0417(9)	−0.122(6)	−0.066(2)	−1.03(5)	0.25(3)
0.10	0.276(10)	0.0393(9)	−0.303(15)	−0.105(3)	−1.05(4)	0.88(7)
$N_f = 8400$						
0.05	0.255(7)	0.0430(7)	−0.122(3)	−0.069(2)	−0.94(3)	0.24(1)
0.10	0.269(13)	0.0389(7)	−0.227(12)	−0.104(3)	−1.02(6)	0.55(6)
0.15	0.242(15)	0.0344(13)	−0.544(17)	−0.128(3)	−0.92(7)	1.85(8)
0.20	0.222(6)	0.0260(8)	−0.841(12)	−0.169(3)	−0.87(3)	2.99(6)
0.25	0.187(11)	0.0165(13)	−1.137(10)	−0.201(6)	−0.76(5)	4.16(4)
0.30	0.083(13)	0.0068(8)	−1.352(7)	−0.228(7)	−0.34(5)	5.00(5)
0.40	−0.061(9)	−0.0279(14)	−1.850(6)	−0.399(11)	0.15(4)	6.45(6)
0.50	−0.278(13)	−0.0736(16)	−2.210(9)	−0.611(5)	0.91(5)	7.11(4)
0.60	−0.578(15)	−0.1792(42)	−2.505(5)	−1.198(13)	1.77(7)	5.81(7)
0.70	−0.919(14)	−0.3024(90)	−2.796(8)	−1.622(16)	2.74(10)	5.22(5)

case. The tail corrections to $\partial\cos\theta/\partial\epsilon_{sf}$, calculated via (2) and (12), are smaller than the uncertainty in the measurements as can be seen by comparing tables 2 and 3 and therefore do not affect our results.

From our simulation at $\epsilon_r = 0.1$ in which we increased the range of the solid–fluid interaction with the right-hand side of the wall to $23.89\sigma_{ff}$, we find that the interactions beyond $13.89\sigma_{ff}$ have no observable effect on $\partial\gamma_{sl}/\partial\epsilon_{sf}$.

The contact angles themselves are listed in tables 2 and 3 and are shown in figure 8. This figure gives an accurate estimate of the wetting transition as the point where the $\cos\theta$ data intersect the line $\cos\theta = 1$. The intersection is at a finite angle which indicates the first-order character of the transition. We estimate the wetting transition at $\epsilon_w = 0.52 \pm 0.01$ from these data.

The data are less decisive at the drying side where the $\cos\theta$ data join the line $\cos\theta = -1$ tangentially. The figure suggests a completely dry state at ϵ_r below $\epsilon_r = 0.15$ but does not exclude the possibility of a weak partially dry state such as the $\partial\cos\theta/\partial\epsilon_{sf}$ data display.

We have also calculated the shift in the contact angles when the tail correction (9) is added to the solid–fluid surface tensions. The results are shown in figure 8 from which it can be seen that the correction, growing linearly with ϵ_r, becomes significant close to the wetting transition only. The wetting transition shifts to $\epsilon_w = 0.51 \pm 0.01$ when calculated from these corrected $\cos\theta$ which is a marginal shift.

The consistency between the measurements of $\cos\theta$ and $\partial\cos\theta/\partial\epsilon_{sf}$ has been checked by fitting a cubic spline (shown in figure 7) to the $\partial\cos\theta/\partial\epsilon_{sf}$ data (of the system with $N_f = 8400$) and integrating the fit from the point $\cos\theta = -1$ at $\epsilon_r = 0.05$ onwards to obtain the value for $\cos\theta$ at an arbitrary ϵ_r. The curve thus
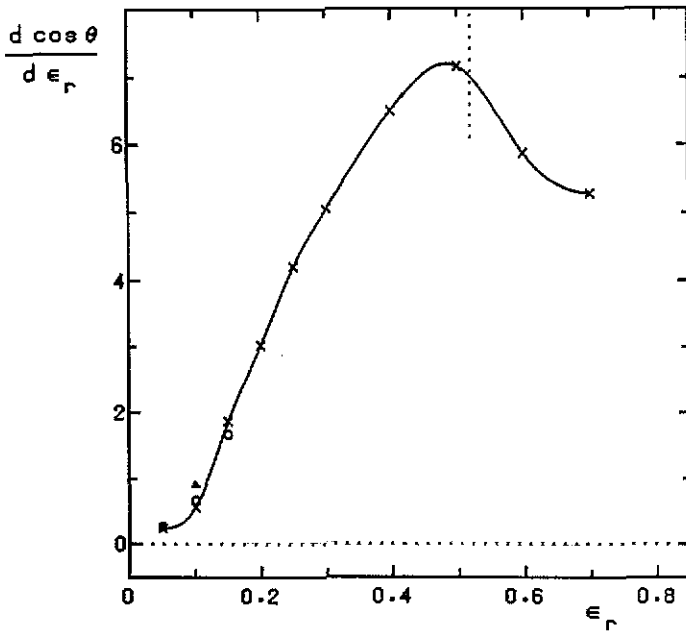
Figure 7. The derivative of the cosine of the contact angle with respect to ϵ_r as a function of ϵ_r. The crosses are obtained with $N_f = 8400$, the open circles represent the branch of increasing ϵ_r, the triangles the branch of decreasing ϵ_r. The system at $\epsilon_r = 0.15$, $N_f = 7297$ has been added to the increasing branch. The error bars have been omitted, they are of the order of the symbol size. The full curve is a cubic spline fit to the data. The vertical dotted line gives the location of the wetting transition.

Table 3. As table 2 but with the tail corrections (given by equations (11) and (12)) added. The errors are the same as the errors in the corresponding entries in table 2.

| ϵ_r	γ_{sl}^*	γ_{sv}^*	$\partial\gamma_{sl}^*/\partial\epsilon_r$	$\partial\gamma_{sv}^*/\partial\epsilon_r$	$\cos\theta$	$\partial\cos\theta/\partial\epsilon_r$
$N_f = 7297$, increasing ϵ_r						
0.05	0.260	0.0400	−0.133	−0.073	−0.98	0.27
0.10	0.249	0.0370	−0.258	−0.108	−0.94	0.67
0.15	0.240	0.0307	−0.511	−0.133	−0.93	1.68
$N_f = 7297$, decreasing ϵ_r						
0.05	0.272	0.0409	−0.129	−0.071	−1.03	0.26
0.10	0.272	0.0376	−0.314	−0.110	−1.04	0.91
$N_f = 8400$						
0.05	0.254	0.0422	−0.128	−0.074	−0.94	0.24
0.10	0.266	0.0372	−0.235	−0.109	−1.02	0.56
0.15	0.238	0.0326	−0.552	−0.131	−0.91	1.87
0.20	0.215	0.0249	−0.851	−0.170	−0.85	3.03
0.25	0.177	0.0151	−1.149	−0.203	−0.72	4.21
0.30	0.069	0.0054	−1.367	−0.230	−0.28	5.05
0.40	−0.076	−0.0295	−1.862	−0.400	0.21	6.50
0.50	−0.298	−0.0756	−2.222	−0.612	0.99	7.16
0.60	−0.605	−0.1812	−2.520	−1.199	1.89	5.87
0.70	−0.950	−0.3047	−2.811	−1.623	2.87	5.28
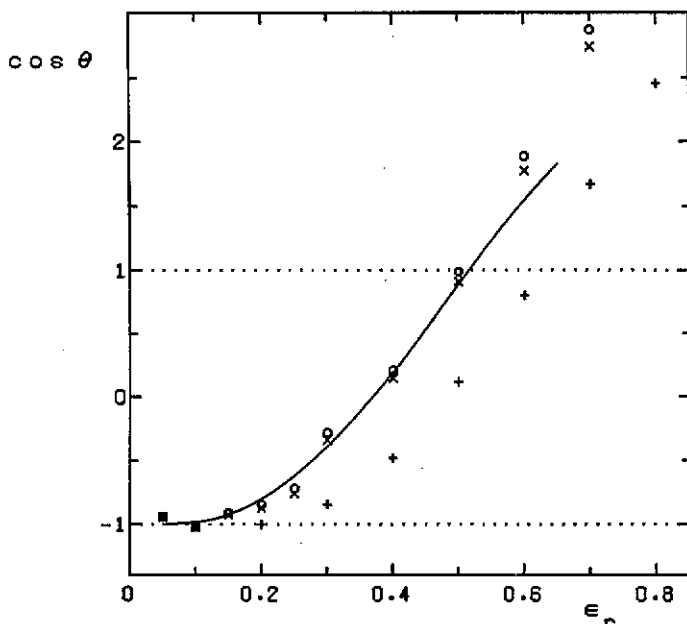
Figure 8. Cosine of the contact angle as a function of ϵ_r. The pluses are obtained for a solid–fluid interface with the interaction between a solid and a fluid particle truncated at $2.35\sigma_{sf}$ [14]. The crosses are obtained in this work from the measurements of the solid–fluid surface tensions with $N_f = 8400$ and do not contain a tail correction. The open circles are obtained by adding the tail correction to the crosses. Error bars are of the order of the symbol size. The full curve is obtained by integrating the fit to the $\partial \cos \theta / \partial \epsilon_{sf}$ data from the point $\cos \theta = -1$ at $\epsilon_r = 0.05$ onwards.

obtained for $\cos \theta$ is given in figure 8. It agrees well with the directly measured angles except for ϵ_r above 0.5 where the decrease of the directly measured $\partial \cos \theta / \partial \epsilon_{sf}$ data in the metastable partially wet state is not accompanied by a corresponding levelling off of the $\cos \theta$ data.

5. Discussion

We have increased the range of the wall–fluid interaction in a system which exhibits a wetting and drying transition in the presence of short-range forces only. It is expected that the long-ranged force facilitates the wetting and prevents the drying transition. We could increase the range of the wall–fluid interaction from $2.35\sigma_{ff}$ to $13.89\sigma_{ff}$ away from the outer layer of the wall. The long-ranged part of the interaction was treated in an approximate way: it was taken to be a Lennard-Jones 9-3 potential and applied each 15th timestep in the simulations but it can reasonably be assumed that these approximations have little effect on the solid–fluid interfaces.

The long-ranged potential is so weak that the bulk character of the liquid and vapour phase is not affected within the accuracy of the simulations. This is not the case for the solid–fluid interfaces where e.g. the coverage clearly increases under the addition of the attractive long-ranged tail. The increase in coverage is most remarkable at the solid–liquid interface where the increase grows with decreasing ϵ_r, indicating the sensitivity of the interface to the wall–fluid potential when the liquid is weakly bound to the wall.

Both the contact angles and their derivatives with respect to ϵ_{sf} increase when the long-ranged tail is added to the system. The wetting transition is located at $\epsilon_w = 0.52\pm0.01$ from the measurements of the contact angle whereas we estimated [14,15] the transition to be at $\epsilon_w = 0.62 \pm 0.02$ for the case without long-ranged potential (where $r_c = 2.35\sigma_{sf}$ for the short-range solid–fluid interaction, as mentioned). The transition retains its strong first-order character. The drying regime is most accurately investigated by the $\partial \cos\theta/\partial\epsilon_{sf}$ measurements. These data suggest that the substrate is partially dry for all ϵ_r although the occurrence of a drying transition at a very small value of ϵ_r cannot be excluded. This value would be below $\epsilon_r = 0.05$ and would thus be much lower than our estimate $\epsilon_d = 0.169 \pm 0.005$ [15] for the substrate without long-ranged substrate-fluid interaction.

The influence of the solid–fluid interaction beyond $13.89\sigma_{ff}$ is not observable in these simulations. The influence can be estimated if one assumes that the omitted interaction does not change the structure of the solid–fluid interface, i.e. the estimate given by (9) and (10). These corrections are vanishingly small at low ϵ_r and hardly change the location of the wetting transition. The simulations at $\epsilon_r = 0.10$ in which we changed the position of z_m^* give further evidence that the forces beyond $13.89\sigma_{ff}$ hardly effect the adsorption behaviour of the slab. Shifting z_m^* to $z_m^* = 10$ one finds that a liquid slab at approximately $16\sigma_{ff}$ away from an attracting substrate, is not adsorbed at the substrate on the timescale of the simulations. Shifting z_m^* to $z_m^* = -10$, it turns out that a liquid slab, adsorbed at a substrate and attracted to it up to $13.89\sigma_{ff}$ away from the substrate, does not move significantly closer to the substrate when the attractive range is increased to $23.89\sigma_{ff}$.

Acknowledgments

References

[1]   Smit B 1990 *Simulation of phase coexistence: from atoms to surfactants PhD Thesis* Rijksuniversiteit Utrecht
[2]   Nijmeijer M J P, Bakker A F, C Bruin and Sikkenk J H 1988 *J. Chem. Phys.* **89** 3789
[3]   Lu B Q, Evans R and Telo da Gama M M 1985 *Mol. Phys.* **55** 1319
[4]   Nightingale M P and Indekeu J O 1985 *Phys. Rev.* B **32** 3364
[5]   Dietrich S 1988 *Phase Transitions and Critical Phenomena* vol 12 ed C Domb and J Lebowitz (London: Academic)
[6]   Brézin E, Halperin B I and Leibler S 1983 *J. Physique* **44** 775
[7]   Dietrich S and Napiórkowski M 1991 *Phys. Rev.* A **43** 1861
[8]   Schick M 1990 *Liquids at Interfaces* ed J Charvolin, J F Joanny and J Zinn-Justin (Amsterdam: North-Holland)
[9]   Durian A J and Franck C 1987 *Phys. Rev.* B **36** 7307
      Léger L and Silberzan P 1990 *J. Phys.: Condens. Matter* **2** 421
[10] Sokolowski S and Fisher J 1990 *Phys. Rev.* A **41** 6866
[11] Henderson J R and van Swol F 1990 *J. Phys.: Condens. Matter* **2** 4537
      van Swol F and Henderson J R 1991 *Phys. Rev.* A **43** 2932 and references therein

Adams P and Henderson J R 1991 *Mol. Phys.* **73** 1383

[12] Sikkenk J H, Indekeu J O, van Leeuwen J M J, Vossnack E O and Bakker A F 1988 *J. Stat. Phys.* **52** 23

[13] Nijmeijer M J P, Bruin C, Bakker A F and van Leeuwen J M J 1989 *Physica* A **160** 166

[14] Nijmeijer M J P, Bruin C, Bakker A F and van Leeuwen J M J 1990 *Phys. Rev.* A **42** 6052

[15] Nijmeijer M J P, Bruin C, Bakker A F and van Leeuwen J M J 1991 *Phys. Rev.* B **44** 834

[16] Finn R 1986 *Equilibrium Capillary Surfaces* (Berlin: Springer)

[17] Saville G 1977 *J. Chem. Soc. Faraday Trans.* **12** 1122

[18] Rowlinson J S and Widom B 1982 *Molecular Theory of Capillarity* (Oxford: Clarendon).

[19] Bakker A F and Bruin C 1988 *Special Purpose Computers* ed B J Alder (London: Academic)

[20] Steele W A 1973 *Surf. Sci.* **36** 317